

Automatic prostate cancer detection through DCE-MRI images: all you need is a good normalization

Guillaume Lemaître^{a,b,*}, Robert Martí^b, Fabrice Meriaudeau^{a,c}

^a*LE2I UMR6306, CNRS, Arts et Métiers, Univ. Bourgogne Franche-Comté, 12 rue de la Fonderie, 71200 Le Creusot, France*

^b*ViCOROB, Universitat de Girona, Campus Montilivi, Edifici P4, 17071 Girona, Spain*

^c*CISIR, Electrical & Electronic Engineering Department, Universiti Teknologi Petronas, 32610 Seri Iskandar, Perak, Malaysia*

Abstract

This template helps you to create a properly formatted L^AT_EX manuscript.

Keywords: DCE-MRI, prostate cancer, normalization, classification, quantification

1. Introduction

Prostate Cancer (PCa) is the second most frequently diagnosed men cancer, accounting for 899,000 cases leading to 258,100 deaths (Ferlay et al., 2010). As highlighted by the PI-RADS Steering Committee, the two main challenges
5 to be addressed are (Weinreb et al., 2016): (i) the improvement of detecting clinically significant PCa and (ii) an increase of the confidence in benign or dormant cases, avoiding unnecessary invasive medical exams. In this regard, multiparametric Magnetic Resonance Imaging (MRI) (mp-MRI) is frequently
10 used to build robust Computer-Aided Detection and Diagnosis (CAD) systems to detect, localize, and grade PCa. In general, CAD systems are based on mp-MRI which potentially combines several of the following modalities (Lemaître et al., 2015): T₂ Weighted (T₂-W)-MRI, Dynamic Contrast-Enhanced (DCE)-MRI, Apparent Diffusion Coefficient (ADC) maps, and Magnetic Resonance Spectroscopy Imaging (MRSI).

*Corresponding author.

Email address: g.lemaitre58@gmail.com (Guillaume Lemaître)

15 In DCE-MRI, a contrast media is injected intravenously and a set of images is acquired over time. Consequently, each voxel in an image corresponds to a dynamic signal which is related to both contrast agent concentration and the vascular properties of the tissue. Therefore, changes of the enhanced signal allows to discriminate healthy from PCa tissues. In fact, these properties are automat-
20 ically extracted using quantitative or semi-quantitative approaches (Lemaître et al., 2015).

Quantitative approaches uses pharmacokinetic modelling based on a bicompart-
ment model, namely Brix (Brix et al., 1991) and Tofts (Tofts et al., 1995) models. The parameters of the Brix model are inferred assuming a linear rela-
25 tionship between the media concentration and the MRI signal intensity. This assumption has shown, however, to lead to inaccurately estimate the pharmacokinetic parameters (Heilmann et al., 2006). In the contrary, Tofts model requires a conversion from MRI signal intensity to concentration, which become a non-linear relationship using specific equation of MRI sequences (e.g., FLASH
30 sequence). Tofts modelling suffers, however, from an higher complexity (Gliozzi et al., 2011). Indeed, the conversion using the non-linear approach requires to acquire a T_1 map which is not always possible during clinical examination. Additionally, the parameter calculation requires the Arterial Input Function (AIF) which is challenging to measure and can also lead to inaccurate estimation.

35 *Semi-quantitative* approaches are rather mathematical than pharmacokinetic modelling (Huisman et al., 2001; Gliozzi et al., 2011). These methods offer the advantages to not require any knowledge about the MRI sequence nor any conversion from signal intensity to concentration. However, the heuristic approach propose by Huisman et al. requires an estimate regarding the noise standard
40 deviation of the signal as well as manual tuning.

Nevertheless, all presented methods suffer from two major drawbacks: (i) inter-patient variability and (ii) loss of information. The inter-patient variability is mainly due to the acquisition process and consequently lead to generalization issue while applying machine learning algorithm. All previous methods extract
45 few discriminative parameters to describe the DCE-MRI signal which might

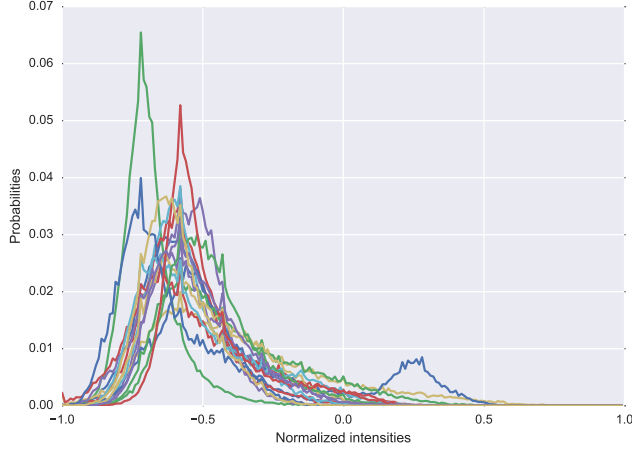


Figure 1: Illustration of the inter-patient variations in 17 different patients, using the PDF representation.

lead to a loss of information.

In this work, we propose a fully automatic normalization method for DCE-MRI that reduce the inter-patient variability of the data. The benefit of our approach will be shown while using quantitative and semi-quantitative approaches.

50 Additionally, we show that using the whole normalized DCE-MRI signal is preferable to quantitative and semi-quantitative methods, leading to the best classification performance.

The paper is organized as follows: Section 2.1 presents into details our normalization strategy for DCE-MRI data. Quantitative and semi-quantitative
55 methods are summarized in Sect. 2.2 with insights about their implementations. Section 3 gives information about the dataset used and provided source code. Experiments and results to answer the previous stated challenges are reported in Sect. 4 while discussed in Sect. 5, followed by a concluding section.

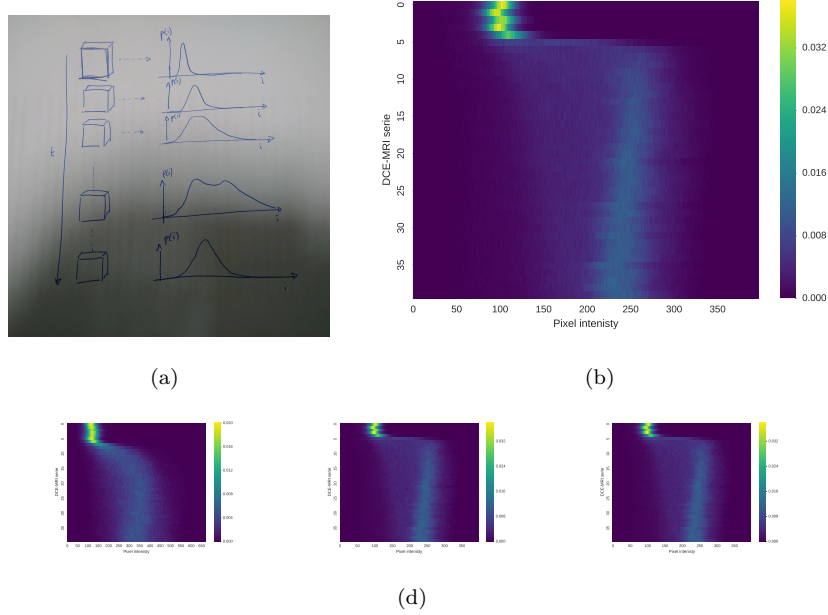


Figure 2: Illustration of the variations of the intensity PDF over time of two patients in a DCE-MRI.

2. Methods

2.1. Normalization of DCE-MRI images

In this work, we propose a method to normalize DCE-MRI prostate data to reduce intra-patient variations, although it can be applied to any DCE-MRI sequences. In T_2 -W-MRI, these variations are characterized by a shift and a scaling of the intensities as illustrated by the intensity Probability Density Function (PDF) in Fig. 1. Therefore, these variations can be corrected using a z -score approach, assuming that the data follow a specific distribution (Lemaitre et al., 2016).

In DCE-MRI, the intensity PDF does not follow a unique type of distribution such as Rician or Gaussian distribution, as shown in Fig. 2(a). Indeed, the inter-patient variations are more complex due to the temporal acquisition. A better representation to observed these variations is to represent the intensity PDF of the DCE-MRI data over time (see Fig. 2(a)) using a heatmap representation as

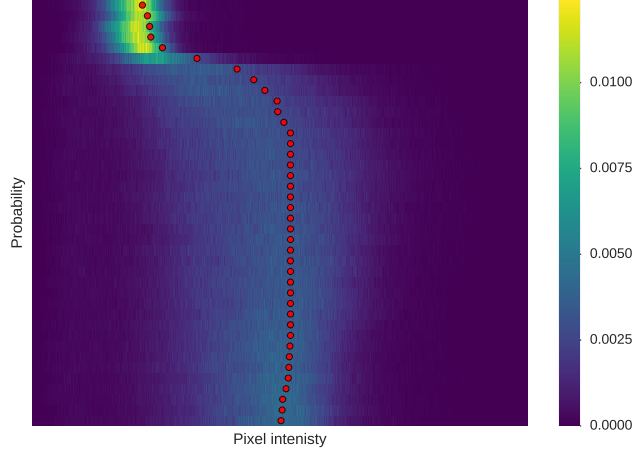


Figure 3: Illustration of the estimator found using the shortest-path through the graph.

shown in Fig. 2(b). Analyzing this heatmap representation across patients (see Fig. 2(d)), the following variations are highlighted: (i) an intensity offset Δ_i of the PDF peak at pre-contrast, (ii) a time offset Δ_t depending of the contrast agent arrival, and (iii) a change of scale σ_i related to the signal enhancement. Therefore, our normalization method should attenuate all these variations and be performed globally across the different time sequence rather than for each independent sequence.

2.1.1. Graph-based offset correction for each DCE-MRI sequence

Before to standardize each sequence, the first step of the normalization is to cancel the intensity specific at each patient, occurring due to the media injection. As previously mentioned, the intensity PDF do not always follow either a Rician or a Gaussian distribution over time, in DCE-MRI. Therefore, the mean of these distributions cannot be used as a potential estimate for this offset. Additionally, this offset should be characterized by a smooth transition between series over time. Thus, this problem is solved using the graph-theory: considering the intensity PDF over time as shown in Fig. 2(b), the offset is the boundary splitting the heatmap in two partitions such that it is as close as possible to the peak of the intensity PDF (see Fig. 3 for an illustration). Given

the heatmap, a directed weighted graph $\mathcal{G} = (\mathcal{V}, \mathcal{E})$ is built by taking each bar of the heatmap as a node and connecting each pair of bars by an edge. The edge weight w_{ij} between two nodes i and j corresponding to two pixels at position (x_i, y_i) and (x_j, y_j) , respectively, is defined as in Eq. (1):

$$w_{ij} = \begin{cases} \alpha \exp(1 - \frac{H(i)}{\max(H)}) & \text{if } x_j = x_i + 1 \text{ and } y_j = y_i, \\ (1 - \alpha) \exp(1 - \frac{H(i)}{\max(H)}) & \text{if } x_j = x_i \text{ and } y_j = y_i + 1, \\ 0 & \text{otherwise,} \end{cases} \quad (1)$$

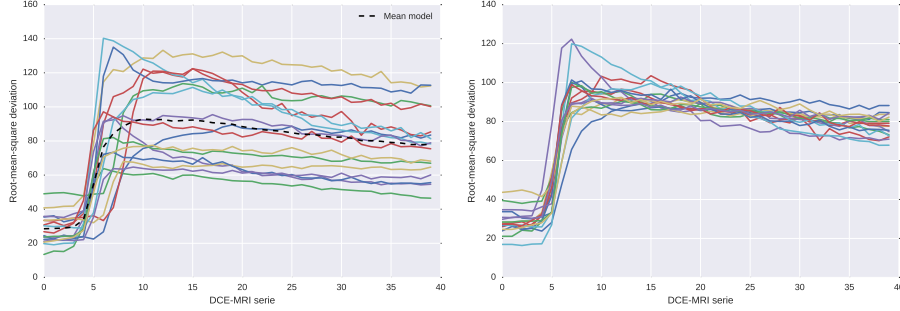
95 where H is the heatmap, α is a smoothing parameter controlling the partitioning.

Therefore, the offset is estimated by finding the shortest-path to cross the graph using Dijkstra's algorithm. The entry and exiting nodes are set to be the bin with the maximum probability for the first DCE-MRI serie and the bin
100 corresponding to the median value for the last DCE-MRI serie, respectively. To ensure a robust estimation of the offset, the process of finding the shortest-path is iteratively repeated by shifting the data and updating the heatmap as well as the graph \mathcal{G} . The procedure is stopped once that the offset found do not change. In general, this process is not repeated more than 3 iterations. An
105 example of the offset found using this approach is presented in Fig. 3. Finally, for each DCE-MRI serie, the intensities are shifted by this offset.

2.1.2. Time offset and data dispersion correction

The next variations to correct are the time offset and the data dispersion. By computing the Root-Mean-Square Deviation (RMSD) of the intensities for each
110 DCE-MRI serie, one can observed these two variations as shown in Fig. 4(a). Therefore, to correct these variations, we propose to register each patient RMSD to a mean model which corresponds to the mean of all patients RMSD. The parametric model to perform the registration is formulated as in Eq. (2):

$$T(\alpha, \tau, f(t)) = \alpha f(t - \tau), \quad (2)$$



(a) RMSD computed for each patient of our dataset. (b) RMSD after alignment using the curve parametric model.

Figure 4: Illustration of the correction of the time offset and the data dispersion.

where α and τ are the two parameters handling the time offset and global scale,
 115 respectively, $f(\cdot)$ is the RMSD function.

Therefore the registration problem is equivalent to:

$$\arg \min_{\alpha, \tau} = \sum_{t=0}^N [T(\alpha, \tau, f(t)) - \mu(t)]^2, \quad (3)$$

where $\mu(\cdot)$ is the mean model, N is the number of DCE-MRI serie.

Illustration of the correction applied to each RMSD patient is shown in
 Fig. 4(b). Once all these parameters have been inferred, the data can be shifted
 120 as well as scaled.

2.2. Quantification of DCE-MRI

As stated in the introduction, one of our main challenge is to demonstrate
 the benefit of using our normalization method prior to extract parameters using
 quantitative and semi-quantitative methods. In this section, we summarize the
 125 different methods which have been used for the quantification of DCE-MRI for
 PCa detection (Lemaître et al., 2015). Furthermore, we would like to emphasize
 the following additional contributions: (i) a novel automatic AIF estimation
 algorithm based on clustering and (ii) a simplified semi-quantitative method
 using constrained optimization.

130 *2.2.1. Brix and Hoffmann models*

In the Brix model (Brix et al., 1991), the MRI signal intensity is assumed to be proportional to the media concentration. Therefore, the model is expressed as in Eq. (4):

$$s_n(t) = 1 + A \left[\frac{\exp(k_{el}t') - 1}{k_{ep}(k_{ep} - k_{el})} \exp(-k_{el}t) - \frac{\exp(k_{ep}t') - 1}{k_{el}(k_{ep} - k_{el})} \exp(-k_{ep}t) \right], \quad (4)$$

with

$$s_n(t) = \frac{s(t)}{S_0}, \quad (5)$$

135 where $s(t)$ and S_0 are the MRI signal intensity at time t and the average pre-contrast MRI signal intensity, respectively; A , k_{el} , and k_{ep} are a constant proportional to the transfer constant, the diffusion rate constant, and the rate constant, respectively. Additionally, t' is set such that $0 \leq t \leq \tau$, $t' = t$ and afterwards while $t > \tau$, $t' = \tau$.

140 Hoffmann et al. propose a similar model as expressed in Eq. (6), which derive from the Brix model:

$$s_n(t) = 1 + \frac{A}{\tau} \left[\frac{k_{ep}(\exp(k_{el}t') - 1)}{k_{el}(k_{ep} - k_{el})} \exp(-k_{el}t) - \frac{\exp(k_{ep}t') - 1}{(k_{ep} - k_{el})} \exp(-k_{ep}t) \right]. \quad (6)$$

The parameters A , k_{el} , and k_{ep} are estimated by fitting the model using non-linear least-squares optimization solved with Levenberg-Marquardt.

2.2.2. Tofts model

145 The extended Tofts model is formulated as in Eq. (7):

$$C_t(t) = K_{trans}C_p(t) * \exp(-k_{ep}t) + v_pC_p(t), \quad (7)$$

where $*$ is the convolution operator; $C_t(t)$ and $C_p(t)$ is the concentration of contrast agent in the tissue and in the plasma, respectively; K_{trans} , k_{ep} , and v_p are the volume transfer constant, the diffusion rate constant, and the plasma volume fraction, respectively.

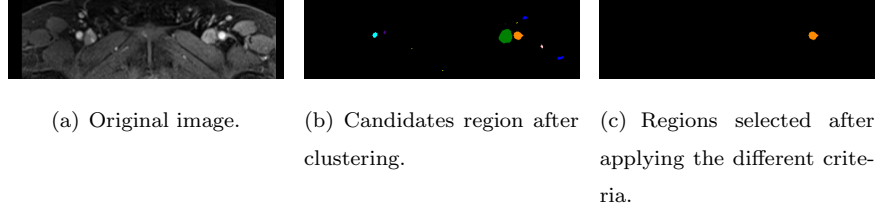


Figure 5: Illustration of the segmentation of the area used to determine the AIF.

Therefore, Tofts model requires to: (i) detect candidate voxels from the femoral or iliac arteries and estimate a patient-based AIF signal, (ii) convert the MRI signal intensity (i.e., AIF and dynamic signal) to a concentration, and (iii) in the case of a population-based AIF, estimate an AIF signal.

Segmentation of artery voxels and patient-based AIF estimation

AIF signal from DCE-MRI can be manually estimated by selecting the most-enhanced voxels from the femoral or iliac arteries (Meng et al., 2010). Few methods have been proposed to address the automated extraction of AIF signal. Chen et al. filter successively the possible candidates (Chen et al., 2008): (i) dynamic signals with small peak are rejecting by thresholding, (ii) voxels with a small wash-in are rejected by thresholding, (iii) a blob detector is used and large enough regions are kept, and (iv) circular and cylindrical criteria are used to reject the last false positive. Zhu et al. propose an iterative method selecting voxels which best fit a gamma variate function (Zhu et al., 2011). However, it requires to compute first and second derivatives as well as maximum curvature points. Shanbhag et al. propose a 4-steps algorithm (Shanbhag et al., 2012; Fennessy et al., 2015): (i) remove slices with artefacts and find the best slices based on intrinsic anatomic landmarks and enhancement characteristics, (ii) find the voxel candidates using the maximum enhanced voxels and a multi-label maximum entropy based thresholding algorithm, (iii) excluding region next to the endorectal coil, and (iv) selecting the best 5 candidates which meet enhancement characteristics and that are correlated.

All the above methods are rather complex and thus we propose a method
 which is based on the following simple assumptions: (i) all possible AIF
 signal candidates should have a similar shape, (ii) an high enhancement,
 and (iii) the arteries should be almost round and within a size range.
 Therefore, each slice is clustered into regions using K-means clustering
 with $k = 6$. The cluster with the highest enhancement—i.e. corresponding
 to the 90th percentile of the maximum of each dynamic signal—contain the
 arteries and is selected. Finally, regions with an eccentricity smaller than
 0.5 and an area in the range of $[100, 400]$ voxels are kept. Additionally,
 to remove voxels contaminated by partial volume effect, only the 10%
 most enhanced voxels of the possible candidates are kept as proposed
 by (Schabel and Parker, 2008) and the average signal is computed. A
 summary of the different segmentation steps is presented in Fig. 5.

Conversion of MRI signal intensity to concentration To estimate the free
 parameters of the Tofts model (see Eq. (7)), the concentration $C_t(t)$ and
 $C_p(t)$ need to be computed from the MRI signal intensity and the AIF sig-
 nal, respectively. This conversion is based on the equation of the FLASH
 sequence—see Appendix A for details—and is formulated as in Eq. (8):

$$c(t) = \frac{1}{TR \cdot r_1} \ln \left(\frac{1 - \cos \alpha \cdot S^* \frac{s(t)}{S_0}}{1 - S^* \frac{s(t)}{S_0}} \right) - \frac{R_{10}}{r_1}, \quad (8)$$

with,

$$S^* = \frac{1 - \exp(-TR \cdot R_{10})}{1 - \cos \alpha \cdot \exp(-TR \cdot R_{10})}, \quad (9)$$

where $s(t)$ is the MRI signal, S_0 is the MRI signal prior to the injection of
 the contrast media, α is the flip angle, TR is the Repetition Time (TR),
 R_{10} is the pre-contrast tissue relaxation time also equal to $\frac{1}{T_{10}}$, r_1 is the
 relaxativity coefficient of the contrast agent.

T_{10} can be estimated from the acquisition of a T_1 map. However, this
 modality is not part of the clinical trial in this research and the value of
 T_{10} is fixed to 1600 ms for both blood and prostate, in accordance with the

values found in the literature (Fennessy et al., 2015; De Bazelaire et al., 2004; Carr and Carroll, 2011).

Estimation of population-based AIF While estimating the pharmacokinetic parameters from Tofts model, the AIF concentration $C_p(t)$ can be computed either from the patient or a population. We presented in the two previous sections the algorithms which allows to estimate the patient-based AIF concentration. To compare with the previous approach, we also computed a population-based AIF which will be also later used to compare the performance of both approaches. In that regard, the population-based AIF was estimated as in (Meng et al., 2010) by fitting the average patient-based AIFs to the model of Parker et al. (2006) which is formulated as in Eq. (10):

$$C_p(t) = \sum_{n=1}^2 \frac{A_n}{\sigma_n \sqrt{2\pi}} \exp\left(\frac{-(t - T_n)^2}{2\sigma_n^2}\right) + \frac{\alpha \exp(-\beta t)}{1 + \exp -s(t - \tau)}, \quad (10)$$

where A_n , T_n , and σ_n are the scaling constants, centers, and widths of the n^{th} Gaussian, α and β are the amplitude and decay constant of the exponential; and s and τ are the width and center of the sigmoid function, respectively.

The parameters are estimated by fitting the model using non-linear least-squares optimization solved with Levenberg-Marquardt.

2.2.3. PUN model

Gliozzi et al. show that Phenomenological Universalities (PUN) approach can be used for DCE-MRI analysis (Gliozzi et al., 2011). The model has been successfully used in a CAD system proposed by Giannini et al. (2015). This model can be expressed as in Eq. (11):

$$s_n(t) = \exp\left[rt + \frac{1}{\beta}(a_0 - r)(\exp(\beta t) - 1)\right], \quad (11)$$

with

$$s_n(t) = \frac{s(t) - S_0}{S_0}, \quad (12)$$

where $s(t)$ and S_0 are the MRI signal intensity at time t and the average pre-contrast MRI signal intensity, respectively; r , a_0 , and β are the free parameters of the model.

210 The parameters are estimated by fitting the model using non-linear least-squares optimization solved with Levenberg-Marcquardt.

2.2.4. Semi-quantitative analysis

The semi-quantitative analysis of the DCE-MRI is equivalent to extract curve characteristics directly from the signal without a strict theoretical pharmacokinetic meaning. In this work, we use the model presented by Huisman
215 et al. (2001) which formulate the MRI signal as in Eq. (13):

$$s(t) = \begin{cases} S_0 & 0 \leq t \leq t_0 \\ S_M - (S_M - S_0) \exp\left(\frac{-(t-t_0)}{\tau}\right) & t_0 < t \leq t_0 + 2\tau \\ S_M - (S_M - S_0) \exp\left(\frac{-(t-t_0)}{\tau}\right) + w(t - t_0 + 2\tau) & t > t_0 + 2\tau \end{cases} \quad (13)$$

where $s(t)$ is the MRI signal intensity, S_0 is the pre-contrast signal intensity, t_0 is the time corresponding to the start of enhancement, S_M and τ is the maximum of the signal and the exponential time constant, and w is the slope of the linear
220 part.

Huisman et al. argue that curve fitting via least-squares minimization using Nelder-Mead algorithm leads to inaccurate estimation of the free parameters: mainly the issue come from an incorrect estimation of the start of enhancement t_0 leading to incorrect estimation of the other parameters. Therefore, they
225 propose to: (i) estimate robustly t_0 , (ii) estimate S_0 by averaging the samples between 0 and t_0 (ii) estimate w depending if the slope is significant or not, (iii)

estimate S_M which should be the point at the intersection of the most probable slope line and the plateau.

Instead of these successive estimations, we propose a unified optimization in which t_0 is fixed since that this is a key parameter. Therefore, t_0 is robustly estimated from the AIF signal since that this is the most enhanced signal in which the start of enhancement is easily identifiable. The AIF signal is computed as in Section 2.2.2. t_0 is estimated by finding the maximum in the beginning of the first derivative of the MRI signal. Then, the function in Eq.(13) is fitted using non-linear least squares with Trust Region Reflective algorithm. Furthermore, the parameters τ and S_M are bounded during the optimization to ensure robust estimations.

From Eq.(13), the following features are extracted: (i) the wash-in corresponding to the slope between t_0 and $t_0 + 2\tau$, (ii) the wash-out corresponding to the parameter w , (iii) the area under the curve between t_0 and the end of the signal, (iv) the exponential time constant τ , and (v) the relative enhancement $S_M - S_0$.

3. Materials

3.1. Data

The multi-parametric MRI data are acquired from a cohort of patients with higher-than-normal level of Prostate-Specific Antigen (PSA). The acquisition is performed using a 3T whole body MRI scanner (Siemens Magnetom Trio TIM, Erlangen, Germany) using sequences to obtain T₂-W-MRI, DCE-MRI and Diffusion Weighted (DW)-MRI. Aside of the MRI examination, these patients also have underwent a guided-biopsy. The dataset is composed of a total of 20 patients of which 18 patients have biopsy proven PCa and 2 patients are “healthy” with negative biopsies. Therefore, 13 patients have a PCa in the Peripheral Zone (PZ), 3 patients have PCa in the Central Gland (CG), 2 patients have invasive PCa in both PZ and CG and finally 2 patients are considered as “healthy”. An experienced radiologist has segmented the prostate organ — on

T₂-W-MRI and DCE-MRI — as well as the prostate zones (i.e., PZ and CG) and PCa on the T₂-W-MRI.

A 3 mm slice fat-suppressed T₂-W fast spin-echo sequence (TR/Echo Time (TE)/Echo Train Length (ETL): 3400 ms/85 ms/13) is used to acquire images in
260 sagittal and oblique coronal planes, the latter planes being orientated perpendicular or parallel to the prostate PZ rectal wall axis. Three-dimensional T₂-W fast spin-echo (TR/TE/ETL: 3600 ms/143 ms/109, slice thickness: 1.25 mm) images are then acquired in an oblique axial plane. The nominal matrix and Field Of View (FOV) of the 3D T₂-W fast spin-echo images are 320 × 256 and
265 280 × 240 mm², respectively, thereby affording sub-millimetric pixel resolution within the imaging plane.

DCE-MRI is performed using a fat suppressed 3D T₁ VIBE sequence (TR/TE/Flip angle: 3.25 ms/1.12 ms/10°; Matrix: 256 × 192; FOV: 280 × 210 (with 75% rectangular FOV); slab of 16 partitions of 3.5 mm thickness; temporal resolution:
270 6 s/slab over approximately 5 min). A power injector (Medrad, Indianola, USA) is used to provide a bolus injection of Gd-DTPA (Dotarem, Guerbet, Roissy, France) at a dose of 0.2 ml Gd-DTPA/kg of body weight.

These DCE-MRI sequences are resampled using the spatial information of the T₂-W-MRI and missing data are interpolated using a linear interpolation.
275 The volumes of the DCE-MRI dynamic are rigidly registered, to remove any patient motion during the acquisition. Furthermore, a non-rigid registration is performed between the T₂-W-MRI and DCE-MRI in order to propagate the prostate zones and PCa ground-truths. The resampling is implemented in C++ using the Insight Segmentation and Registration Toolkit (Ibanez et al., 2005).

280 3.2. Implementation

The implementation of the registration (C++), normalization (Python), and classification pipeline (Python) are publicly available on GitHub¹. The data

¹<https://github.com/I2Cvb/lemaitre-2016-nov/tree/master>

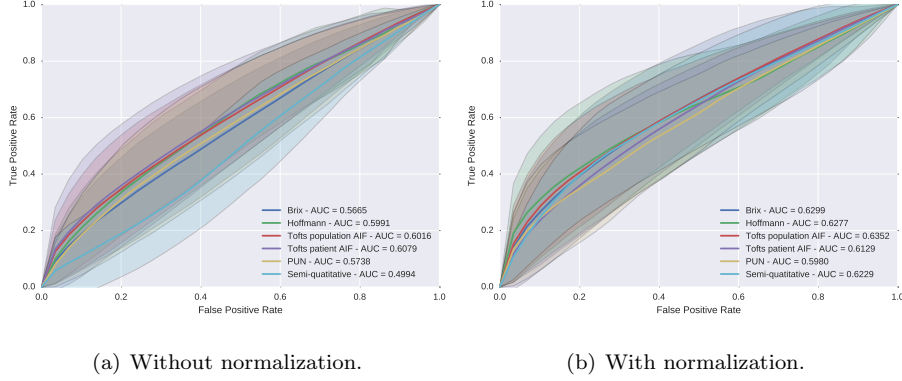


Figure 6: ROC analysis using a RF classifier with and without normalization DCE-MRI data for different pharmacokinetic models.

used for this work are also publicly available².

4. Experiments and results

4.1. Classification of individual parameter for each model

This experiment consists in assessing the benefit of normalizing the DCE-MRI, prior to classify each individual parameter for each model. Therefore, a Gaussian Naive Bayes (NB) classifier is used in conjunction with a Leave-One-Patient-Out Cross-Validation (LOPO CV). The results are summarized in Table 1. In general, data normalization leads to better classification performance while extracting pharmacokinetic related parameters. Only the PUN model does not follow this tendency. **Find out why!!!**

4.2. Classification by combining the parameters for each model

In previous proposed CAD systems, the pharmacokinetic of a single model are combined. Therefore, for each model, all parameters are combined and classified using a Random Forest (RF) classifier in a LOPO CV fashion. The use

²<http://kaggle.com>

Table 1: AUC for each individual pharmacokinetic parameter using a NB classifier.

Features	Un-normalized data	Normalized data
Brix model		
A	0.62	0.67
k_{el}	0.52	0.61
k_{ep}	0.52	0.58
Hoffmann model		
A	0.50	0.56
k_{el}	0.53	0.64
k_{ep}	0.50	0.66
Tofts model with population AIF		
K_{trans}	0.62	0.65
v_e	0.50	0.52
v_p	0.63	0.53
Tofts model with patient AIF		
K_{trans}	0.66	0.65
v_e	0.50	0.52
v_p	0.37	0.65
PUN model		
a_0	0.53	0.51
r	0.59	0.55
β	0.56	0.44
Semi-quantitative analysis		
wash-in	0.64	0.51
wash-out	0.50	0.66
IAUC	0.61	0.64
τ	0.57	0.61
$S_M - S_0$	0.63	0.64

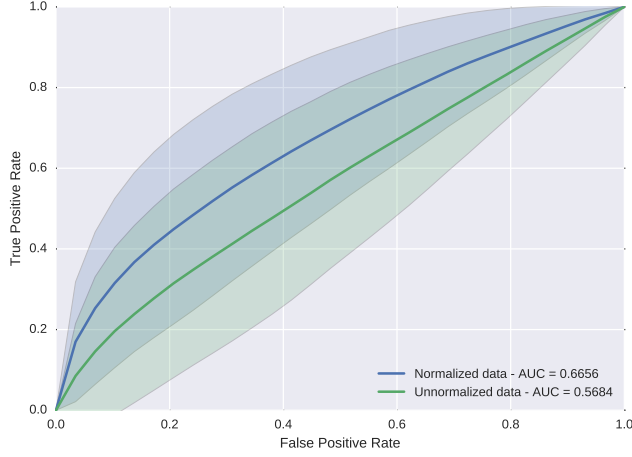


Figure 7: ROC analysis using the entire DCE-MRI signal with and without normalization in conjunction with a RF classifier.

of RF is motivated since that it leads to the best performance in the state-of-the-art methods (Litjens et al., 2014). Results are summarized by performing a Receiver Operating Characteristic (ROC) analysis and computing the Area Under the Curve (AUC), as reported in Fig. 6. Independently to the quantification
 300 model, the data normalization improves the AUC and classification performance.

4.3. Classification of the entire enhanced DCE-MRI signal

As stated in the introduction, the quantification methods are extracting a set of parameters characterizing the enhancement DCE-MRI signal. However, this
 305 extraction could lead to a loss of information. This experiment is performed to assess if making use of the whole DCE-MRI signal instead of the just the pharmacokinetic parameters can improve the classification performance. Therefore, each enhanced DCE-MRI signal, normalized and un-normalized, is classified using a RF classifier in a LOPO CV fashion. The ROC analysis and AUC are
 310 reported in Fig. 7. It can be noted that the worst performance are achieved while classifying raw data without normalization. However, data normalization in conjunction with the use of the whole DCE-MRI signal is the strategy which outperforms all others.

5. Discussions

- 315 • Discuss about the T1 parameters in Tofts and say that we can do better probably.
- Compare the two approach for the AIF.
- Make a discussion about the detailed interpretation of individual feature classification. There is something to discuss about the semi-quantitative
320 from wash-in to wash-out reversed performance. Something also about the PUN model.
- Explain the drawbacks of the whole signal classification (time).

6. Conclusions and future works

In this work, we presented a new method for normalizing/standardizing
325 DCE-MRI data. Through different experiments, we show the benefit of such normalization. Furthermore, we show that using the whole DCE-MRI signal instead extracting parameters lead to the best classification performance.

As avenues for future research, this normalization has to be part of a mp-MRI CAD system, mixing T₂-W-MRI, DCE-MRI, DW-MRI, and MRSI.

330 Appendix A. Conversion from FLASH signal to media concentration

In this appendix, we show the demonstration used to extract the agent concentration from the MRI signal.

The signal equation in FLASH sequence (Haase et al., 1986) is defined as:

$$s(t) = S_{eq} \sin \alpha \cdot \frac{1 - \exp(-TR(R_{10} + r_1 c(t)))}{1 - \cos \alpha \cdot \exp(-TR(R_{10} + r_1 c(t)))}, \quad (\text{A.1})$$

where $s(t)$ is the MRI signal, S_{eq} is the maximum signal amplitude of the spoiled
335 gradient at the TE which is proportional to the Proton Density (PD), α is the flip angle, TR is the Repetition Time (TR), R_{10} is the pre-contrast tissue relaxation

time also equal to $\frac{1}{T_{10}}$, r_1 is the relaxitivity coefficient of the contrast agent, and $c(t)$ is the media concentration.

Therefore, the pre-contrast signal prior to bolus injection of the media is
 340 defined as:

$$S_0 = S_{eq} \sin \alpha \cdot \frac{1 - \exp(-TR \cdot R_{10})}{1 - \cos \alpha \cdot \exp(-TR \cdot R_{10})}. \quad (\text{A.2})$$

To simplify the demonstration, let us define:

$$A = \exp(-TR \cdot R_{10}), \quad (\text{A.3})$$

$$B = \exp(-TR \cdot r_1 c(t)). \quad (\text{A.4})$$

Let us define:

$$S^* = \frac{S_0}{S_{eq} \sin \alpha}, \quad (\text{A.5})$$

$$= \frac{1 - A}{1 - A \cos \alpha}. \quad (\text{A.6})$$

Thus,

$$S^* \frac{s(t)}{S_0} = \frac{S_0}{S_{eq} \sin \alpha} \frac{s(t)}{S_0}, \quad (\text{A.7})$$

$$= \frac{1 - AB}{1 - AB \cos \alpha}. \quad (\text{A.8})$$

Now, let us define:

$$\frac{1 - \cos \alpha \cdot S^* \frac{s(t)}{S_0}}{1 - S^* \frac{s(t)}{S_0}} = \frac{1 - \cos \alpha \left(\frac{1-AB}{1-AB \cos \alpha} \right)}{1 - \frac{1-AB}{1-AB \cos \alpha}}, \quad (\text{A.9})$$

$$= \frac{1 - AB \cos \alpha - \cos \alpha (1 - AB)}{1 - AB \cos \alpha - (1 - AB)}, \quad (\text{A.10})$$

$$= \frac{1 - AB \cos \alpha - \cos \alpha + AB \cos \alpha}{1 - AB \cos \alpha - 1 + AB}, \quad (\text{A.11})$$

$$= \frac{1 - \cos \alpha}{AB(1 - \cos \alpha)}, \quad (\text{A.12})$$

$$= \frac{1}{AB}. \quad (\text{A.13})$$

345 Thus,

$$-TR \cdot R_{10} - TR \cdot r_1 c(t) = \ln \left(\frac{1 - \cos \alpha \cdot S^* \frac{s(t)}{S_0}}{1 - S^* \frac{s(t)}{S_0}} \right). \quad (\text{A.14})$$

Therefore,

$$c(t) = \frac{1}{TR \cdot r_1} \ln \left(\frac{1 - \cos \alpha \cdot S^* \frac{s(t)}{S_0}}{1 - S^* \frac{s(t)}{S_0}} \right) - \frac{R_{10}}{r_1}. \quad (\text{A.15})$$

References

- Brix, G., Semmler, W., Port, R., Schad, L.R., Layer, G., Lorenz, W.J., 1991. Pharmacokinetic parameters in cns gd-dtpa enhanced mr imaging. Journal of computer assisted tomography 15, 621–628.
- 350 Carr, J.C., Carroll, T.J., 2011. Magnetic resonance angiography: principles and applications. Springer Science & Business Media.
- Chen, J., Yao, J., Thomasson, D., 2008. Automatic determination of arterial input function for dynamic contrast enhanced mri in tumor assessment, in: International Conference on Medical Image Computing and Computer-Assisted Intervention, Springer. pp. 594–601. doi:10.1007/978-3-540-85988-8_71.
- 355 De Bazelaire, C.M., Duhamel, G.D., Rofsky, N.M., Alsop, D.C., 2004. Mr imaging relaxation times of abdominal and pelvic tissues measured in vivo at

- 3.0 t: preliminary results 1. *Radiology* 230, 652–659. doi:10.1148/radiol.
 2303021331.
- 360 Fennessy, F.M., Fedorov, A., Penzkofer, T., Kim, K.W., Hirsch, M.S., Vangel,
 M.G., Masry, P., Flood, T.A., Chang, M.C., Tempany, C.M., et al., 2015.
 Quantitative pharmacokinetic analysis of prostate cancer dce-mri at 3t: com-
 parison of two arterial input functions on cancer detection with digitized whole
 365 mount histopathological validation. *Magnetic resonance imaging* 33, 886–894.
 doi:10.1016/j.mri.2015.02.008.
- Ferlay, J., Shin, H.R., Bray, F., Forman, D., Mathers, C., Parkin, D.M., 2010.
 Estimates of worldwide burden of cancer in 2008: Globocan 2008. *Interna-
 tional journal of cancer* 127, 2893–2917. doi:10.1002/ijc.25516.
- 370 Giannini, V., Mazzetti, S., Vignati, A., Russo, F., Bollito, E., Porpiglia, F.,
 Stasi, M., Regge, D., 2015. A fully automatic computer aided diagnosis system
 for peripheral zone prostate cancer detection using multi-parametric magnetic
 resonance imaging. *Computerized Medical Imaging and Graphics* 46, 219–226.
 doi:10.1016/j.compmedimag.2015.09.001.
- 375 Gliozzi, A., Mazzetti, S., Delsanto, P.P., Regge, D., Stasi, M., 2011. Phe-
 nomenological universalities: a novel tool for the analysis of dynamic contrast
 enhancement in magnetic resonance imaging. *Physics in medicine and biology*
 56, 573.
- Haase, A., Frahm, J., Matthaei, D., Hanicke, W., Merboldt, K.D., 1986. Flash
 380 imaging. rapid nmr imaging using low flip-angle pulses. *Journal of Magnetic
 Resonance (1969)* 67, 258–266. doi:10.1016/0022-2364(86)90433-6.
- Heilmann, M., Kiessling, F., Enderlin, M., Schad, L.R., 2006. Determination of
 pharmacokinetic parameters in dce mri: consequence of nonlinearity between
 contrast agent concentration and signal intensity. *Investigative radiology* 41,
 385 536–543. doi:10.1097/01.rli.0000209607.99200.53.

- Hoffmann, U., Brix, G., Knopp, M.V., Heß, T., Lorenz, W.J., 1995. Pharmacokinetic mapping of the breast: a new method for dynamic mr mammography. *Magnetic resonance in medicine* 33, 506–514. doi:10.1002/mrm.1910330408.
- 390 Huisman, H.J., Engelbrecht, M.R., Barentsz, J.O., 2001. Accurate estimation of pharmacokinetic contrast-enhanced dynamic mri parameters of the prostate. *Journal of Magnetic Resonance Imaging* 13, 607–614. doi:10.1002/jmri.1085.
- Ibanez, L., Schroeder, W., Ng, L., Cates, J., 2005. The itk software guide .
- 395 Lemaître, G., Dastjerdi, M.R., Massich, J., Vilanova, J.C., Walker, P.M., Freixenet, J., Meyer-Baese, A., Mériaudeau, F., Marti, R., 2016. Normalization of t2w-mri prostate images using rician a priori, in: *SPIE Medical Imaging, International Society for Optics and Photonics*. pp. 978529–978529. doi:10.1117/12.2216072.
- 400 Lemaître, G., Martí, R., Freixenet, J., Vilanova, J.C., Walker, P.M., Meriaudeau, F., 2015. Computer-aided detection and diagnosis for prostate cancer based on mono and multi-parametric mri: A review. *Computers in biology and medicine* 60, 8–31. doi:10.1016/j.combiomed.2015.02.009.
- 405 Litjens, G., Debats, O., Barentsz, J., Karssemeijer, N., Huisman, H., 2014. Computer-aided detection of prostate cancer in mri. *IEEE transactions on medical imaging* 33, 1083–1092. doi:10.1109/TMI.2014.2303821.
- Meng, R., Chang, S.D., Jones, E.C., Goldenberg, S.L., Kozlowski, P., 2010. Comparison between population average and experimentally measured arterial input function in predicting biopsy results in prostate cancer. *Academic radiology* 17, 520–525. doi:10.1016/j.acra.2009.11.006.
- 410 Parker, G.J., Roberts, C., Macdonald, A., Buonaccorsi, G.A., Cheung, S., Buckley, D.L., Jackson, A., Watson, Y., Davies, K., Jayson, G.C., 2006.

- Experimentally-derived functional form for a population-averaged high-temporal-resolution arterial input function for dynamic contrast-enhanced mri. *Magnetic resonance in medicine* 56, 993–1000. doi:10.1002/mrm.21066.
- Schabel, M.C., Parker, D.L., 2008. Uncertainty and bias in contrast concentration measurements using spoiled gradient echo pulse sequences. *Physics in medicine and biology* 53, 2345. doi:10.1088/0031-9155/53/9/010.
- Shanbhag, D., Gupta, S.N., Rajamani, K., Zhu, Y., Mullick, R., 2012. A generalized methodology for detection of vascular input function with dynamic contrast enhanced perfusion data, in: *ISMRM*, p. 10.
- Tofts, P.S., Berkowitz, B., Schnall, M.D., 1995. Quantitative analysis of dynamic gd-dtpa enhancement in breast tumors using a permeability model. *Magnetic Resonance in Medicine* 33, 564–568. doi:10.1002/mrm.1910330416.
- Weinreb, J.C., Barentsz, J.O., Choyke, P.L., Cornud, F., Haider, M.A., Macura, K.J., Margolis, D., Schnall, M.D., Shtern, F., Tempany, C.M., et al., 2016. PIRADS prostate imaging-reporting and data system: 2015, version 2. *European urology* 69, 16–40.
- Zhu, Y., Chang, M.C., Gupta, S., 2011. Automated determination of arterial input function for dce-mri of the prostate, in: *SPIE Medical Imaging*, International Society for Optics and Photonics. pp. 79630W–79630W. doi:10.1117/12.878213.